

Stark manifold ultraviolet emission in Gd-implanted β -Ga₂O₃ thin films

Martin S. Williams^{a,b}, Mahmoud Elhajhasan^{a,b}, Marco Schowalter^{a,b}, Lewis Penman^c, Alexander Karg^{a,b}, Patrick Vogt^{a,d}, Fabien C.-P. Massabuau^e, Andreas Rosenauer^{a,b}, Gordon Callsen^{a,b}, Carsten Ronning^e, Martin Eickhoff^{a,b}, Manuel Alonso-Orts^{a,b}

^a Institute of Solid State Physics, University of Bremen, Otto-Hahn-Allee 1, 28359 Bremen, Germany

^b MAPEX Center for Materials and Processes, University of Bremen, Bibliothekstraße 1, 28359 Bremen, Germany

^c Department of Physics, SUPA, University of Strathclyde, Glasgow, G4 0NG, United Kingdom

^d Max Planck Institute for Solid State Research, 70569 Stuttgart, Germany

^e Institute of Solid State Physics, Friedrich Schiller University Jena, Helmholtzweg 3, 07743 Jena, Germany

ARTICLE INFO

Keywords:

Ultra-wide band gap
Gallium oxide
Gd³⁺
Rare-earth ion
Ion implantation
Ultraviolet
Photoluminescence

ABSTRACT

Gadolinium (Gd) is a promising optically active lanthanide for UV emission. In this work, the optical emission properties of Gd-implanted monoclinic gallium oxide (β -Ga₂O₃) thin films are investigated. Second phase formation (γ -Ga₂O₃) is observed due to implantation-induced damage of the β -Ga₂O₃ lattice. Annealing the implanted films results in various β -Ga₂O₃ grain orientations. The relationship between the crystalline nature and the optical properties of the β -Ga₂O₃:Gd³⁺ films is studied. Optical activation occurs after annealing at 700 °C, revealing a photoluminescence (PL) band at 3.92 eV. This emission is attributed to the ⁶P_{7/2} → ⁸S_{7/2} transition of Gd³⁺ in β -Ga₂O₃. Its four constituent emission components at 3.9118 eV, 3.9153 eV, 3.9221 eV and 3.9348 eV, due to the ion's ⁶P_{7/2} Stark splitting in the β -Ga₂O₃ crystal field, are investigated. The transition energies are independent of annealing temperature and film growth method, highlighting the insensitivity of the 4f⁷ orbital to minor changes in the monoclinic crystal environment.

1. Introduction

Monoclinic gallium oxide (β -Ga₂O₃) is an ultra-wide band gap material ($E_g = 4.8$ eV) exhibiting promising performance in high-power electronics [1] and optics [2]. In optical applications such as waveguides, for example, β -Ga₂O₃ exhibits loss values comparable to other wide band gap materials [3]. The native material's suitability as an optical emitter, however, remains hindered by the defect nature of its broad emission band, which extends from the near-UV to the green spectral range [4,5].

Due to its wide transparency range and chemical stability [6], β -Ga₂O₃ is a good host for optically active ions. Previous works have studied the emission of doped Ga₂O₃ in the different visible spectral ranges, from the red (Eu³⁺, Cr, Co, Sm) to the blue (Eu²⁺, Dy) [7], for their use in, e.g., luminescent thermometry [8]. However, a predominant UV emission in Ga₂O₃ has rarely been reported [9,10]. By optically active ion doping, the only option to enhance the UV emission in β -Ga₂O₃ is gadolinium (Gd³⁺) [9]. This ion in YAl₃(BO₃)₄:Pr³⁺ was recently demonstrated as a Boltzmann thermometer in the 30 K to 800 K range [11].

The material with the greatest understanding as a host for Gd³⁺ in previous research is wurtzite AlN, showing an emission peak around

3.9 eV from the ⁶P_{7/2} → ⁸S_{7/2} ion excited level to ion ground state transition (see Fig. 1). It consists of four separate transitions due to the Stark splitting of the ⁶P_{7/2} manifold [12–16]. In AlN:Gd³⁺, a large ionic radius mismatch exists between Al³⁺ and Gd³⁺: 0.54 Å [17] and 0.94 Å [18], respectively. This mismatch is reduced, however, when considering β -Ga₂O₃:Gd³⁺, with a Ga³⁺ ionic radius of 0.62 Å [19]. Nogales et al. activated emission attributed to the ⁶P_{7/2} → ⁸S_{7/2} transition in Gd³⁺-implanted β -Ga₂O₃ pellets and nanowires, exhibiting higher emission energy than for AlN:Gd³⁺ [20]. Furthermore, López et al. qualitatively observed the Stark splitting of the ⁶P_{7/2} manifold in β -Ga₂O₃:Gd³⁺ nanowires [21], although precise values for the energy splitting could not be resolved [20,21]. Indeed, systematic studies investigating the effect of the monoclinic crystal field on rare-earth-doped β -Ga₂O₃ and other crystal structures are lacking.

In this work, β -Ga₂O₃ thin films grown by plasma-assisted molecular beam epitaxy (MBE) and atomic layer deposition (ALD) were implanted with Gd³⁺ and subsequently annealed at increasing annealing temperatures (T_{ann}). The lattice recovery and emission from the ⁶P_{7/2} → ⁸S_{7/2} transition are studied and the energy splitting of the four transitions is

* Corresponding author.

E-mail addresses: marwilli@uni-bremen.de (M.S. Williams), alonsoor@uni-bremen.de (M. Alonso-Orts).

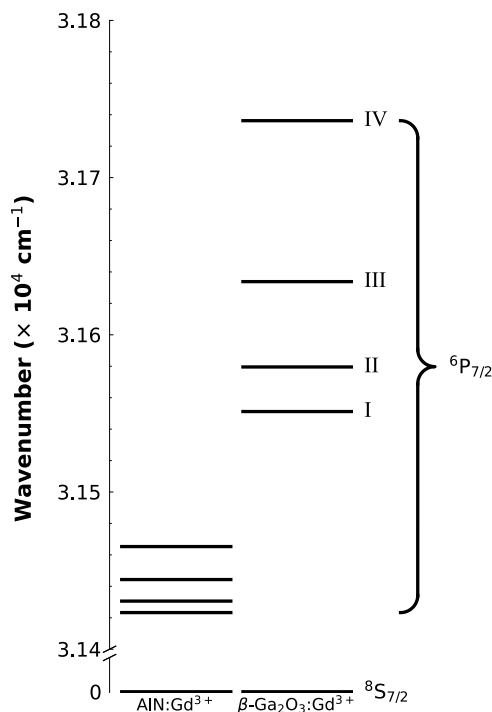


Fig. 1. Energy band diagram for AlN:Gd^{3+} (values reported by Gruber et al. [13]) and $\beta\text{-Ga}_2\text{O}_3\text{:Gd}^{3+}$ (values reported in this work). The sublevels of the ${}^6\text{P}_{7/2}$ manifold are labelled I-IV, corresponding to the peak labels used in later figures.

resolved with high precision. The stability of the four levels of the ${}^6\text{P}_{7/2}$ Stark manifold in $\beta\text{-Ga}_2\text{O}_3\text{:Gd}^{3+}$ is discussed.

2. Experimental details

A $\beta\text{-Ga}_2\text{O}_3$ thin film was grown by MBE on a 2-inch $\alpha\text{-Al}_2\text{O}_3(0001)$ substrate with an average thickness measured by reflectometry of (87 ± 9) nm over an area of $2 \times 2 \text{ cm}^2$. The wafer was subsequently diced into $1 \times 1 \text{ cm}^2$ samples for implantation. Additionally, an amorphous Ga_2O_3 thin film was grown by ALD on an $\alpha\text{-Al}_2\text{O}_3(0001)$ substrate with a film thickness of (91 ± 2) nm as measured by reflectometry. Additional information on film growth can be found in the supplementary material.

Gd was implanted in the films with an ion energy of 130 keV, tilted 7° from the surface normal to avoid channelling. A summary of the implanted films, ion fluences and implantation temperatures (T_{im}) is presented in Table 1. Monte Carlo simulations using the SRIM software package [22,23] result in an ion range of about 26 nm and a corresponding straggling of approximately 9 nm. The peak Gd concentrations of the simulated Gaussian-like implantation profiles are $2.25 \times 10^{21} \text{ cm}^{-3}$ and $4.5 \times 10^{21} \text{ cm}^{-3}$ for the two ion fluences, as also indicated in Table 1, which are an order of magnitude below the Ga concentration in $\beta\text{-Ga}_2\text{O}_3$ ($3.82 \times 10^{22} \text{ cm}^{-3}$). The Gd concentration profile for this implantation in $\beta\text{-Ga}_2\text{O}_3$ is shown in the supplementary material, Fig. S1. It should be noted that, while the concentration profile can be affected by implantation temperature, the diffusion of hydrogen implanted $\beta\text{-Ga}_2\text{O}_3$ has only been observed at implantation temperatures higher than 450°C [24]. Heavier elements exhibit lower diffusivity still. Therefore, no significant redistribution of the Gd is expected when implanted at 300°C compared to room temperature.

The implanted films were annealed in a Jipelec JetFirst 100 rapid thermal annealing system. Six one-minute annealing steps were carried out from 400°C to 900°C for each sample in 100°C steps in Ar atmosphere.

A Philips X'Pert Pro-MRD system using $\text{Cu K}\alpha_1$ radiation was employed for high-resolution X-ray diffraction (HRXRD). Scanning transmission electron microscopy (STEM) images and energy dispersive X-ray (EDX) maps were recorded using a ThermoFisher Spectra300 equipped with a high brightness gun, an aberration corrector for the condenser lens and a SuperX EDX detector. The TEM was operated at a 300 kV acceleration voltage employing a beam current of approximately 200 pA, which was selected using its monochromator. STEM images were recorded with the Fischione HAADF detector at a camera length of approximately 91 mm. TEM specimens were prepared by FIB lift-out in an FEI Nova200.

Micro-Raman (μ -Raman) measurements were performed using a Kimmon HeCd laser (442 nm excitation wavelength) and a Horiba LabRAM HR Evolution confocal spectrometer while using an Olympus LMPLFLN 100 \times objective (NA = 0.8).

Photoluminescence (PL) measurements of the samples were performed after excitation with a Clark-MXR Inc. Magellan-5 pulsed Yb-fiber laser with an excitation wavelength of 257 nm and repetition rate of 13.15 MHz. The PL signal was collected by the same confocal spectrometer that also enabled the μ -Raman measurements while using a Thorlabs LMM40X-UVV 40 \times objective (NA = 0.5). Overview and detailed PL spectra were measured using optical gratings with 100 l/mm and 1800 l/mm, respectively, the latter aligned to the Si Raman peak at 520.7 cm^{-1} [25]. All PL spectra were corrected for the system response. Temperature-dependent PL was performed using an Oxford Instruments MicrostatHiRes cryostat with liquid He as a coolant and a Mitutoyo M Plan UV 50 \times objective (NA = 0.4). Additional details on the PL measurement process and measurement precision are discussed in the supplementary material.

Cathodoluminescence (CL) was measured in an FEI Quanta 250 FEG scanning electron microscope, in tandem with an Oriol 1/8 m (Model 77400) spectrograph with a 2400 l/mm ruled diffraction grating blazed at 250 nm and a cooled Andor Newton DU970-UVB EMCCD camera.

3. Results and discussion

The crystalline nature of the samples after growth, implantation and annealing was first determined by μ -Raman and symmetric HRXRD, shown in Fig. 2(a,b). The MBE-grown thin films, samples 1 and 2, exhibit the A_g^3 (202 cm^{-1}) and A_g^5 (348 cm^{-1}) $\beta\text{-Ga}_2\text{O}_3$ Raman modes [26, 27] and the $(\bar{4}02)$ $\beta\text{-Ga}_2\text{O}_3$ X-ray diffraction peak directly after growth, while the ALD-grown sample 3 is amorphous (not shown).

All three samples exhibit no $\beta\text{-Ga}_2\text{O}_3$ Raman modes after implantation. The $\beta\text{-Ga}_2\text{O}_3$ diffraction peak is also not detected for sample 3, indicating the sample has remained amorphous after implantation. Conversely, an additional diffraction peak centred at $2\theta = 37.8^\circ$ is observed in the HRXRD spectra for sample 1 and, with lower intensity, sample 2. This is attributed to diffraction from the (222) $\gamma\text{-Ga}_2\text{O}_3$ plane, formed due to an implantation-induced partial phase transition. The γ phase of Ga_2O_3 is typically regarded as a 'defect' phase, often associated with point defects present after ion implantation [28,29].

Annealing at temperatures between 400°C and 600°C is not sufficient to observe substantial $\beta\text{-Ga}_2\text{O}_3$ lattice recovery, as no change in the μ -Raman and HRXRD diffraction spectra could be observed (not shown). After annealing at $T_{\text{ann}} = 700^\circ \text{C}$, however, the A_g^3 mode is measured again for samples 1 and 3. In sample 1, the recovery of the $\beta\text{-Ga}_2\text{O}_3$ lattice is also observed in the HRXRD spectrum, which exhibits a lower diffraction angle ($2\theta = 38.0^\circ$) than the as-grown sample ($2\theta = 38.25^\circ$). This is attributed to tensile strain induced by implantation. Contrarily, the $(\bar{4}02)$ $\beta\text{-Ga}_2\text{O}_3$ diffraction peak is not measured for sample 3 at $T_{\text{ann}} = 700^\circ \text{C}$ despite the presence of the A_g^3 Raman mode, indicating that sample 3 is highly polycrystalline at this T_{ann} .

The $(\bar{4}02)$ $\beta\text{-Ga}_2\text{O}_3$ diffraction peak is detected for all samples at $T_{\text{ann}} = 800^\circ \text{C}$ as the implanted films exhibit an increase in long-range structural order, with increased intensity at $T_{\text{ann}} = 900^\circ \text{C}$. At the

Table 1
Summary of the implantation parameters used for all samples investigated in this work. RT = room temperature.

| Sample No. | Growth method | Ion fluence ($\times 10^{15} \text{ cm}^{-2}$) | Peak Gd concentration ($\times 10^{21} \text{ cm}^{-3}$) | T_{im} ($^{\circ}\text{C}$) |
|------------|---------------|--|--|--|
| 1 | MBE | 5 | 2.25 | 300 |
| 2 | MBE | 10 | 4.5 | RT |
| 3 | ALD | 10 | 4.5 | RT |

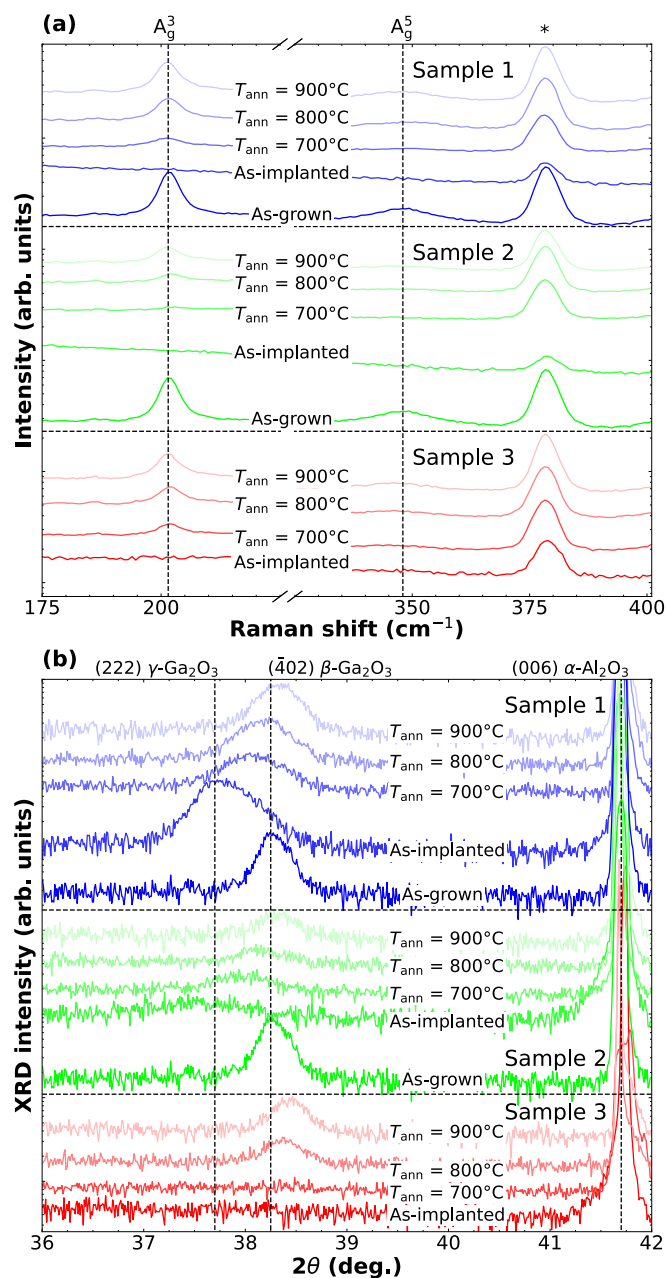


Fig. 2. (a) μ -Raman spectra of the studied samples, showing the A_g^3 and A_g^5 modes of β - Ga_2O_3 . The asterisk denotes the α - Al_2O_3 Raman mode of the underlying substrate. (b) Symmetric HRXRD spectra of Gd-implanted β - Ga_2O_3 annealed at different temperatures. The (222) γ - Ga_2O_3 , (402) β - Ga_2O_3 and (006) α - Al_2O_3 diffraction peaks are marked by vertical dashed lines.

highest T_{ann} , the (402) β - Ga_2O_3 diffraction peak shifts to angles higher than 38.25° in all samples. This is attributed to a decreasing c -lattice parameter as a result of partial Al diffusion from the substrate into the thin films [30,31], which is shown in the STEM analysis below.

In order to better understand such HRXRD peak shift and to gain further insights into the crystalline nature of the films, STEM analysis

was performed at $T_{\text{ann}} = 900^\circ\text{C}$. A cross-sectional STEM-HAADF image measured for sample 1, and the corresponding STEM-EDX linescan and magnified STEM-HAADF images are shown in Fig. 3(a–c). The same STEM measurements but from sample 3 are shown in Fig. 3(d–f). Additionally, STEM-EDX maps for both samples are included in the supplementary material, Fig. S2. The expected (201)-oriented β - Ga_2O_3 HAADF pattern is observed for both samples, but only close to the substrate interface. The HAADF image of sample 1 shows rotational domains in all areas, while the implantation region in sample 3 is found to remain predominantly amorphous up to this annealing temperature. Al diffusion from the substrate to both films is observed as an extended interface at the substrate, particularly in sample 1. Furthermore, an Al metal concentration of < 10 at.% is detected away from the interface in the EDX linescans in Fig. 3(b,e). A peak Gd metal concentration of 5 at.% and 14 at.% is estimated in samples 1 and 3, respectively. The distribution of Gd in sample 1 follows the expected Gaussian-like distribution from SRIM simulations, while the Gd concentration exhibits a second peak in sample 3. This is attributed to Gd out-diffusion through the amorphous layer during the high T_{ann} treatments.

The optical activation of Gd^{3+} and its luminescence in the β - Ga_2O_3 crystal structure were investigated. Fig. 4(a) shows overview room-temperature PL spectra measured on sample 1. At $T_{\text{ann}} = 700^\circ\text{C}$, only a broad band emission is observed. This broad emission, which extends from the near-UV to the green spectral range, is typical of β - Ga_2O_3 and is broadly described as originating from self-trapped holes (UV range), extended defects (blue range), gallium and oxygen vacancies, interstitials or complexes (blue and green ranges), and impurities (usually, green and red ranges) [4,5]. Such emission is dominant in all our samples, however, the presence of an additional PL peak at 3.92 eV is evident after annealing at $T_{\text{ann}} = 900^\circ\text{C}$, as shown in Fig. 4(a). Such luminescence peak originates from the ${}^6\text{P}_{7/2} \rightarrow {}^8\text{S}_{7/2}$ transition of Gd^{3+} [12,13,20,21]. Measuring PL with higher spectral resolution enables a detailed investigation of this transition in β - $\text{Ga}_2\text{O}_3:\text{Gd}^{3+}$. Such spectra reveal that the Gd ion is optically activate from $T_{\text{ann}} = 700^\circ\text{C}$, albeit very weakly and only in samples 1 and 3. Such intensity monotonically increases for all three samples between $T_{\text{ann}} = 700^\circ\text{C}$ and $T_{\text{ann}} = 900^\circ\text{C}$, as shown in Fig. 4(b–d). As displayed in the PL spectra in these figures, which were performed at the same positions under the same conditions for each sample and T_{ann} , the single peak at 3.92 eV is the superposition of emissions from four separate transitions — attributed to the Stark splitting of the ${}^6\text{P}_{7/2}$ manifold in the host crystal field [13] — and is observed in all three samples. The luminescence peaks are correlated to their sublevels in Fig. 1 via the labels I–IV. The sublevel energies remain constant across all samples and T_{ann} at: I - (3.9118 ± 0.0002) eV, II - (3.9153 ± 0.0002) eV, III - (3.9221 ± 0.0002) eV and IV - (3.9348 ± 0.0002) eV. Such energy stability demonstrates that, firstly, the ${}^6\text{P}_{7/2}$ manifold is unaffected by differences to the surrounding crystal environment in the three samples, due to shielding of the $4f^7$ orbital by the distorted 5s and 5p orbitals [32] and, secondly, the emission from the ${}^6\text{P}_{7/2} \rightarrow {}^8\text{S}_{7/2}$ transition is reliant on its immediate crystal environment and not on long-range ordering [see, for example, the different crystal orientations in Fig. 3(d)]. The four peaks were also observed at RT by CL, shown in Fig. S3 in the supplemental material. The measured ${}^6\text{P}_{7/2} \rightarrow {}^8\text{S}_{7/2}$ transition energies, and therefore Stark splitting of the ${}^6\text{P}_{7/2}$ manifold, are identical when measured by CL and PL.

The detailed PL spectra were analysed further by background subtraction, peak curve fitting and combining of results taken from many measurements (detailed in the supplementary material). The FWHM

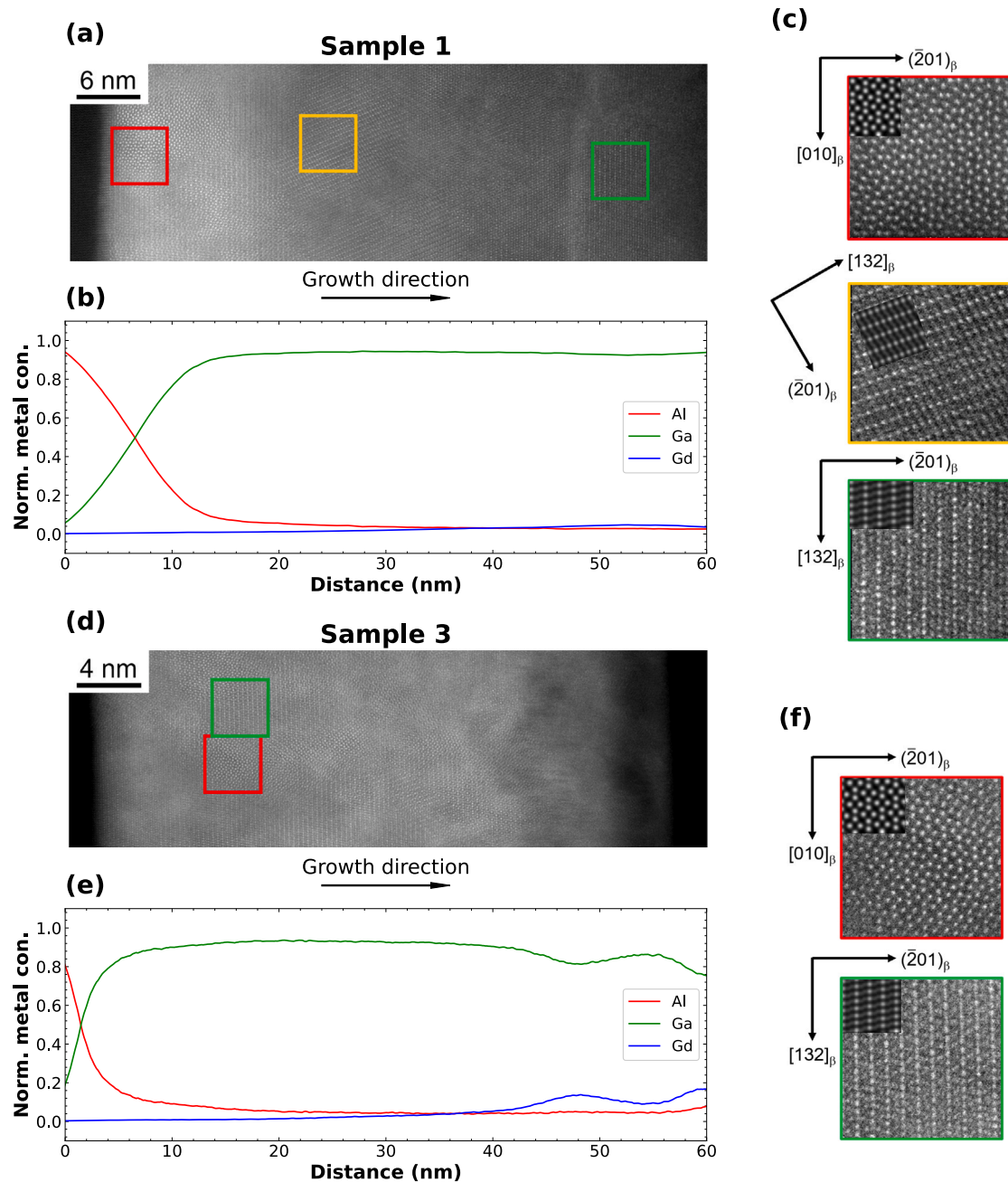


Fig. 3. Sample 1, $T_{\text{ann}} = 900$ °C: (a) Cross-sectional STEM-HAADF image, (b) STEM-EDX linescan and (c) magnified cross-sectional STEM-HAADF with simulated HAADF patterns inset. Sample 3 after a twenty-minute Ar sputtering to remove surface contamination, $T_{\text{ann}} = 900$ °C: (d) Cross-sectional STEM-HAADF image, (e) STEM-EDX linescan and (f) magnified cross-sectional STEM-HAADF with simulated HAADF patterns inset.

values from peak fitting for $T_{\text{ann}} = 900$ °C are shown in Fig. 4(e). A FWHM value ≤ 1.5 meV is measured for the three investigated samples. The minor FWHM differences between the samples correspond to variations in their crystalline order, with sample 1 exhibiting the lowest FWHM of below 1 meV for the three lowest-energy emission sublevels in agreement with the highest absolute PL intensity. Consistent with the STEM measurements in Fig. 3, film synthesis and implantation methods that result in improved crystalline order are required for higher ${}^6\text{P}_{7/2} \rightarrow {}^8\text{S}_{7/2}$ PL intensities.

The PL peak intensities for the main annealing temperatures are summarised in Fig. 4(f). Sample 1 exhibits the highest intensity of all samples in this work despite its lower implantation fluence, being 6 times and 4.5 times higher than the intensity observed in samples 2 and 3, as a result of the increased long-range crystalline order that can be inferred from the STEM-HAADF images in Fig. 3, which underscores

the improvement provided by the implantation conditions of sample 1. This trend was also observed in other material systems. Lee et al. for example, observed an increased activation in ion-implanted Si at higher-than-RT implantation temperatures, attributed to self-annealing reducing damage during implantation [33] (often also named dynamic annealing [34]). A combination of self-annealing and the formation of $\gamma\text{-Ga}_2\text{O}_3$ may contribute to an improved crystalline ordering, and hence an increased emission intensity, in sample 1. Additionally, for sample 3, a 33% higher absolute PL intensity is observed than for sample 2, indicating the initial RT implantation of amorphous Ga_2O_3 thin films may prove beneficial for the fabrication of $\beta\text{-Ga}_2\text{O}_3$ -based optical emitters.

To extract further information about the ${}^6\text{P}_{7/2} \rightarrow {}^8\text{S}_{7/2}$ transition in $\beta\text{-Ga}_2\text{O}_3\text{:Gd}^{3+}$, temperature-dependent PL measurements of sample 1, which are shown for $T_{\text{ann}} = 900$ °C in Fig. 5(a), were undertaken.

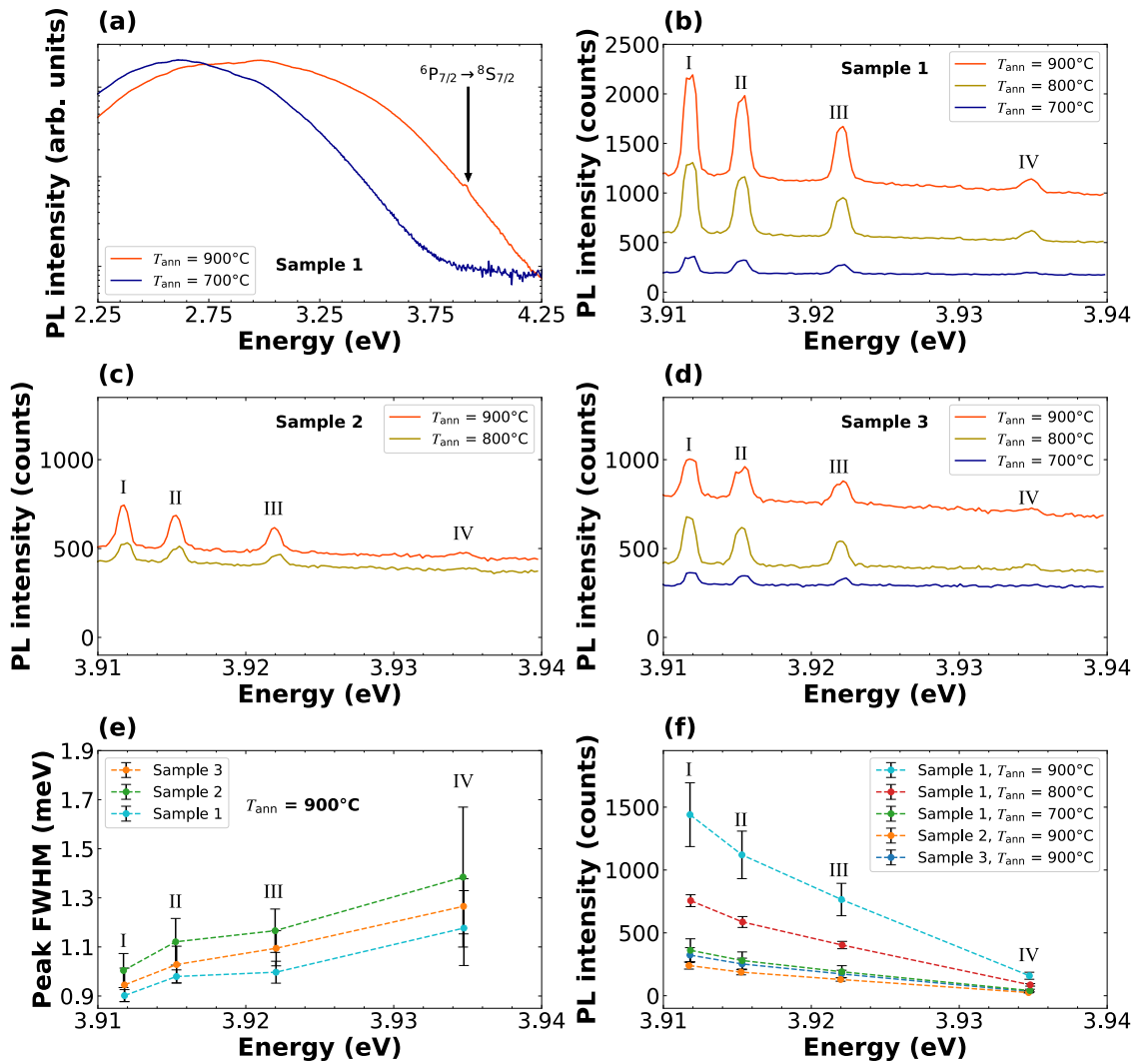


Fig. 4. (a) PL spectra of sample 1 for $T_{\text{ann}} = 700^\circ\text{C}$ and $T_{\text{ann}} = 900^\circ\text{C}$ (arrow marks the ${}^6\text{P}_{7/2} \rightarrow {}^8\text{S}_{7/2}$ transition emission energy). As-measured detailed PL emission spectra on (b) sample 1, (c) sample 2 and (d) sample 3. (e) Peak FWHM comparison between the implanted samples at $T_{\text{ann}} = 900^\circ\text{C}$. (f) Summary of ${}^6\text{P}_{7/2}$ emission intensity from the studied samples and T_{ann} . Peak labels I-IV correspond to the sublevels of the ${}^6\text{P}_{7/2}$ manifold, illustrated in Fig. 1. Dashed lines serve as a guide to the eye.

As the temperature increases from 4 K to 290 K, the Gd^{3+} emission peaks become visible in the order I \rightarrow IV, which is the result of thermal re-population of the ${}^6\text{P}_{7/2}$ manifold sublevels. This is illustrated in Fig. 5(b), where the normalised PL intensity is compared with the calculated sublevel occupation ratio, represented by a Boltzmann distribution [35]:

$$N_i = \exp\left(-\frac{\Delta E_i}{k_B T}\right) / Z(T), \quad (1)$$

where ΔE_i is the energy difference between the i th sublevel and the lowest-energy sublevel of the Stark-split manifold, k_B the Boltzmann constant, T the temperature and $Z(T)$ the partition function of the manifold. The calculated occupation ratios follow the experimental PL intensity in the investigated temperature range, indicating that the PL peak intensities originate from the thermal population of the ${}^6\text{P}_{7/2}$ manifold sublevels, with some deviation observed due to the low intensity of peak IV. Furthermore, the relative peak intensities measured at RT remain the same across all samples (illustrated clearly by normalised peak intensities that can be found in the supplementary material, Fig. S4) meaning that the occupation of the four ${}^6\text{P}_{7/2}$ sublevels remains unchanged independent of the specific sample. The quenching of the ${}^6\text{P}_{7/2} \rightarrow {}^8\text{S}_{7/2}$ PL emission was investigated as shown in the supplementary material, Fig. S5. Only considering the quenching of peak I as an exponential decay yields a quenching activation energy

of 80.9 meV, closely matching the energy of the B_g^5 $\beta\text{-Ga}_2\text{O}_3$ Raman mode [26,27].

Beyond the Gd^{3+} -related peaks, two additional luminescence peaks at 3.924 eV and 3.929 eV are observed for sample 1 at $T_{\text{ann}} = 900^\circ\text{C}$ in the temperature range 4 K to 230 K, marked by asterisks in Fig. 5(a). It is shown in Fig. S6 in the supplementary material that they are observed in ALD- and MBE-grown samples only after Gd^{3+} implantation and annealing. Such reliance on implantation, while not exhibiting the expected temperature-dependence of Stark-split levels, indicates that they do not belong to the ${}^6\text{P}_{7/2}$ manifold of Gd^{3+} but are a result of the ion implantation process, most likely related to the formation of structural defects.

Finally, the ${}^6\text{P}_{7/2} \rightarrow {}^8\text{S}_{7/2}$ sublevel transition energies are compared to values reported in the literature in Fig. 5(c). The energy splitting by the local crystal environment of the ${}^6\text{P}_{7/2}$ manifold in $\beta\text{-Ga}_2\text{O}_3:\text{Gd}^{3+}$ thin films is approximately four times larger than the splitting previously reported in $\text{AlN}:\text{Gd}^{3+}$ [13] and so, too, is the crystal field in $\beta\text{-Ga}_2\text{O}_3$ with respect to AlN. Conversely, the peak positions between this work and López et al. [21] in $\beta\text{-Ga}_2\text{O}_3$ nanowires present a similar Stark splitting while an absolute energy offset is observed, which can be attributed to, for example, different spectral calibrations in experimental setups and/or differences regarding the sample dimensionality.

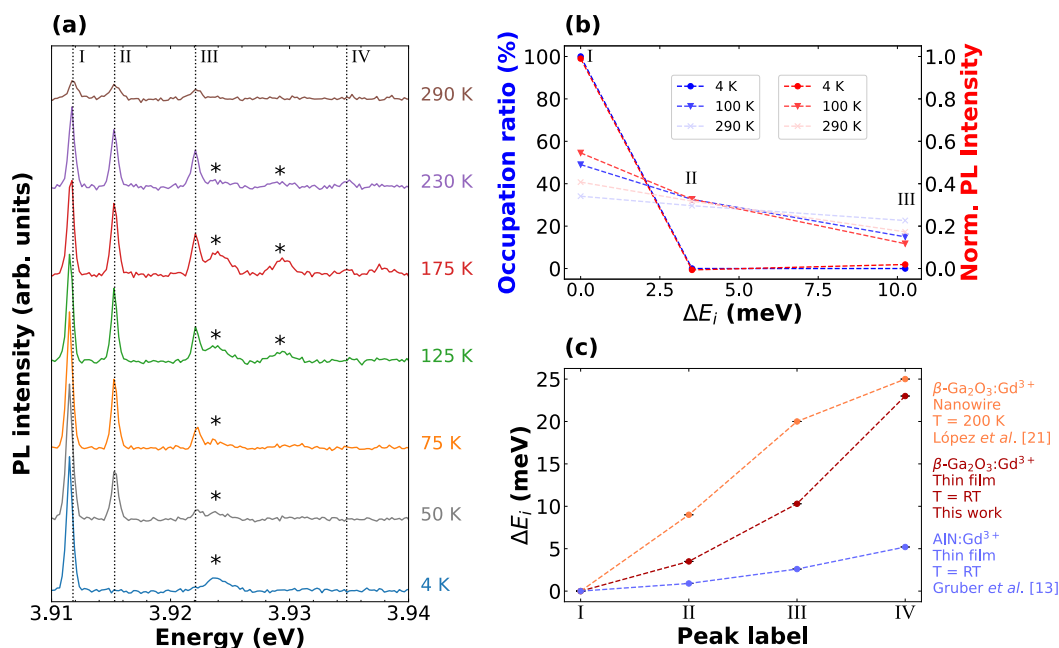


Fig. 5. (a) Temperature-dependent PL spectra measured for sample 1 at $T_{\text{ann}} = 900$ °C. (b) Calculated occupation ratio (blue) and measured normalised PL intensity (red) as a function of sublevel energy, demonstrating the thermal re-population of the higher-energy ${}^6P_{7/2}$ sublevels. (c) Comparison of ${}^6P_{7/2} \rightarrow {}^8S_{7/2}$ luminescence peak splitting with values reported in literature. Peak labels I-IV correspond to the sublevels of the ${}^6P_{7/2}$ manifold as introduced in Fig. 1. Dashed lines serve as a guide to the eye.

4. Conclusion

A well-defined luminescence signal in the UV-B spectral range was activated in implanted $\beta\text{-Ga}_2\text{O}_3:\text{Gd}^{3+}$ thin films grown by MBE and ALD. After implantation, the formation of $\gamma\text{-Ga}_2\text{O}_3$ was observed. Shorter-range ordering of the $\beta\text{-Ga}_2\text{O}_3$ lattice was observed and Gd^{3+} became optically active after annealing at $T_{\text{ann}} = 700$ °C, resulting in four individual PL peaks originating from the Stark-split ${}^6P_{7/2} \rightarrow {}^8S_{7/2}$ transition of Gd^{3+} . Such PL intensity increases, up to an annealing temperature of 900 °C, due to longer-range structural ordering. The positions of the PL peaks at RT, (3.9118 ± 0.0002) eV, (3.9153 ± 0.0002) eV, (3.9221 ± 0.0002) eV and (3.9348 ± 0.0002) eV, were independent of the sample growth method, implantation parameters and annealing temperature. The stability of the four ${}^6P_{7/2}$ sublevels indicates, firstly, that the ${}^6P_{7/2} \rightarrow {}^8S_{7/2}$ transition energy is affected by the local crystal ordering and, secondly, that there is a pronounced shielding of the Gd $4f^7$ orbital. When comparing the results of this work to the reported transition energies in $\text{AlN}:\text{Gd}^{3+}$, the splitting of the ${}^6P_{7/2}$ level, and hence the crystal field, is approximately four times larger in $\beta\text{-Ga}_2\text{O}_3:\text{Gd}^{3+}$. Despite the shielding of the $4f^7$ orbital, the Stark splitting of the ${}^6P_{7/2}$ manifold is nonetheless observed with high precision and provides a direct experimental probe of the crystal field strength — an invaluable tool for future crystal and ligand field theory studies of Gd^{3+} in different host lattices. The thermal population of the ${}^6P_{7/2}$ manifold was observed by temperature-dependent PL measurements. Our results indicate that further optimisation of the long-range crystalline order in $\beta\text{-Ga}_2\text{O}_3:\text{Gd}^{3+}$ layers would pave the way towards $\beta\text{-Ga}_2\text{O}_3$ -based UV-B emitters.

CRedit authorship contribution statement

Martin S. Williams: Writing – review & editing, Writing – original draft, Methodology, Investigation, Formal analysis, Data curation. **Mahmoud Elhajhasan:** Writing – review & editing, Methodology, Investigation. **Marco Schowalter:** Writing – review & editing, Methodology, Investigation. **Lewis Penman:** Writing – review & editing, Methodology, Investigation. **Alexander Karg:** Writing – review & editing, Methodology, Investigation. **Patrick Vogt:** Methodology. **Fabien C.-P.**

Massabuau: Writing – review & editing, Methodology, Investigation. **Andreas Rosenauer:** Writing – review & editing, Methodology, Investigation. **Gordon Callsen:** Writing – review & editing, Methodology, Investigation. **Carsten Ronning:** Writing – review & editing, Methodology, Investigation. **Martin Eickhoff:** Writing – review & editing, Methodology, Funding acquisition, Conceptualization. **Manuel Alonso-Orts:** Writing – review & editing, Writing – original draft, Methodology, Investigation, Funding acquisition, Conceptualization.

Declaration of competing interest

The authors declare that they have no known competing financial interests or personal relationships that could have appeared to influence the work reported in this paper.

Acknowledgments

M. A.-O. acknowledges financial support from the Central Research Development Fund (CRDF) of the University of Bremen (ZF04/2021) and funding from the Deutsche Forschungsgemeinschaft (DFG, German Research Foundation) – Project number = 548722780.

M. E. and G. C. acknowledge funding from the CRDF of the “Universität Bremen” for the project “Joint optical and thermal designs for next generation nanophotonics”.

The research of M. E. and G. C. was further funded by the major research instrumentation program of the DFG (Grant No. 511416444).

G. C. also acknowledges the MAPEX-CF Grant for Correlated Workflows (Grant No. 40401080).

L. P. and F. C.-P. M. acknowledge financial support from the Engineering and Physical Sciences Research Council (EP/W524670/1).

Appendix A. Supplementary data

Supplementary material related to this article can be found online at <https://doi.org/10.1016/j.mtphys.2025.101731>.

Data availability

Data will be made available on request.

References

- [1] M. Higashiwaki, K. Sasaki, H. Murakami, Y. Kumagai, A. Koukitu, A. Kuramata, T. Masui, S. Yamakoshi, Recent progress in Ga₂O₃ power devices, *Semicond. Sci. Technol.* 31 (2016) <http://dx.doi.org/10.1088/0268-1242/31/3/034001>.
- [2] H. Deng, K.J. Leadle, Y. Miao, D.S. Black, K.E. Urbanek, J. McNeur, M. Kozák, A. Ceballos, P. Hommelhoff, O. Solgaard, R.L. Byer, J.S. Harris, Gallium oxide for high-power optical applications, *Adv. Opt. Mater.* 8 (2020) <http://dx.doi.org/10.1002/adom.201901522>.
- [3] J. Zhou, H. Chen, H. Fu, K. Fu, X. Deng, X. Huang, T.H. Yang, J.A. Montes, C. Yang, X. Qi, B. Zhang, X. Zhang, Y. Zhao, Demonstration of low loss β -Ga₂O₃ optical waveguides in the UV-NIR spectra, *Appl. Phys. Lett.* 115 (2019) <http://dx.doi.org/10.1063/1.5133845>.
- [4] M. Alonso-Orts, E. Nogales, B. Méndez, Optical properties of Ga₂O₃ nanostructures, in: F. Ren, S.J. Pearton (Eds.), *Wide Bandgap Semiconductor-Based Electronics*, IOP Publishing, 2020.
- [5] J. Cooke, M. Lou, M.A. Scarpulla, B. Sensale-Rodriguez, Polarized photoluminescence from Sn, Fe, and unintentionally doped β -Ga₂O₃, *J. Vac. Sci. Technol. A* 42 (2) (2024) 022801, <http://dx.doi.org/10.1116/6.0003216>.
- [6] Z. Wu, G. Bai, Q. Hu, D. Guo, C. Sun, L. Ji, M. Lei, L. Li, P. Li, J. Hao, W. Tang, Effects of dopant concentration on structural and near-infrared luminescence of Nd³⁺-doped β -Ga₂O₃ thin films, *Appl. Phys. Lett.* 106 (2015) <http://dx.doi.org/10.1063/1.4919586>.
- [7] D. Guo, Q. Guo, Z. Chen, Z. Wu, P. Li, W. Tang, Review of Ga₂O₃-based optoelectronic devices, *Mater. Today Phys.* 11 (2019) <http://dx.doi.org/10.1016/j.mtphys.2019.100157>.
- [8] M. Alonso-Orts, R.J. Neelissen, D. Carrasco, M. Schowalter, A. Rosenauer, E. Nogales, B. Méndez, M. Eickhoff, Accurate and robust wide-range luminescent microthermometer based on ALD-encapsulated Ga₂O₃:Cr DBR microcavities, *Adv. Mater. Technol.* 10 (1) (2025) 2400881, <http://dx.doi.org/10.1002/admt.202400881>.
- [9] E. Nogales, I. López, B. Méndez, J. Piqueras, K. Lorenz, E. Alves, J.A. García, Doped gallium oxide nanowires for photonics, in: F.H. Teherani, D.C. Look, D.J. Rogers (Eds.), in: *Oxide-Based Materials and Devices III*, vol. 8263, SPIE, International Society for Optics and Photonics, 2012, <http://dx.doi.org/10.1117/12.907766>.
- [10] J. Huso, M.D. McCluskey, Y. Yu, M.M. Islam, F. Selim, Localized UV emitters on the surface of β -Ga₂O₃, *Sci. Rep.* 10 (2020) <http://dx.doi.org/10.1038/s41598-020-76967-6>.
- [11] D. Yu, H. Li, D. Zhang, Q. Zhang, A. Meijerink, M. Suta, One ion to catch them all: Targeted high-precision Boltzmann thermometry over a wide temperature range with Gd³⁺, *Light.: Sci. Appl.* 10 (2021) <http://dx.doi.org/10.1038/s41377-021-00677-5>.
- [12] U. Vetter, J. Zenneck, H. Hofsäss, Intense ultraviolet cathodoluminescence at 318 nm from Gd³⁺-doped AlN, *Appl. Phys. Lett.* 83 (2003) <http://dx.doi.org/10.1063/1.1605237>.
- [13] J.B. Gruber, U. Vetter, H. Hofsäss, B. Zandi, M.F. Reid, Spectra and energy levels of Gd³⁺ (4f⁷) in AlN, *Phys. Rev. B - Condens. Matter Mater. Phys.* 69 (2004) <http://dx.doi.org/10.1103/PhysRevB.69.195202>.
- [14] S. Kitayama, H. Yoshitomi, S. Iwahashi, J. Nakamura, T. Kita, Y. Chigi, T. Nishimoto, H. Tanaka, M. Kobayashi, T. Ishihara, H. Izumi, Influence of local atomic configuration in AlGdN phosphor thin films on deep ultra-violet luminescence intensity, *J. Appl. Phys.* 110 (2011) <http://dx.doi.org/10.1063/1.3658845>.
- [15] Y. Ishizu, K. Tsuji, Y. Harada, T. Kita, Y. Chigi, T. Nishimoto, H. Tanaka, M. Kobayashi, T. Ishihara, H. Izumi, Resonant indirect excitation of Gd³⁺ in AlN thin films, *J. Appl. Phys.* 115 (2014) <http://dx.doi.org/10.1063/1.4874745>.
- [16] T. Kita, Y. Ishizu, K. Tsuji, Y. Harada, Y. Chigi, T. Nishimoto, H. Tanaka, M. Kobayashi, T. Ishihara, H. Izumi, Thermal annealing effects on ultra-violet luminescence properties of Gd doped AlN, *J. Appl. Phys.* 117 (2015) <http://dx.doi.org/10.1063/1.4919419>.
- [17] D.C. Smith, E.-A. Perseil, Sb-rich rutile in the manganese concentrations at St. Marcel-Praborna, Aosta Valley, Italy: petrology and crystal-chemistry, *Miner. Mag.* 61 (1997) 655–669, <http://dx.doi.org/10.1180/minmag.1997.061.408.04>.
- [18] R.A. Pawar, S.M. Patange, A.R. Shitre, S.K. Gore, S.S. Jadhav, S.E. Shirsath, Crystal chemistry and single-phase synthesis of Gd³⁺ substituted Co-Zn ferrite nanoparticles for enhanced magnetic properties, *RSC Adv.* 8 (2018) 25258–25267, <http://dx.doi.org/10.1039/c8ra04282a>.
- [19] R.D. Shannon, C.T. Prewitt, Effective ionic radii in oxides and fluorides, *Acta Crystallogr. Sect. B Struct. Crystallogr. Cryst. Chem.* 25 (1969) 925–946, <http://dx.doi.org/10.1107/S0567740869003220>, URL <https://journals.iucr.org/paper?S0567740869003220>.
- [20] E. Nogales, P. Hidalgo, K. Lorenz, B. Méndez, J. Piqueras, E. Alves, Cathodoluminescence of rare earth implanted Ga₂O₃ and GeO₂ nanostructures, *Nanotechnology* 22 (2011) <http://dx.doi.org/10.1088/0957-4484/22/28/285706>.
- [21] I. López, K. Lorenz, E. Nogales, B. Méndez, J. Piqueras, E. Alves, J.A. García, Study of the relationship between crystal structure and luminescence in rare-earth-implanted Ga₂O₃ nanowires during annealing treatments, *J. Mater. Sci.* 49 (2014) <http://dx.doi.org/10.1007/s10853-013-7811-x>.
- [22] J. Ziegler, J. Biersack, U. Littmark, *Stopping and Range of Ions in Solids*, Pergamon Press, New York, 1985.
- [23] J. Ziegler, J. Biersack, M. Ziegler, SRIM-2013 - The stopping and range of ions in matter, URL www.srim.org.
- [24] R. Sharma, M.E. Law, F. Ren, A.Y. Polyakov, S.J. Pearton, Diffusion of dopants and impurities in β -Ga₂O₃, *J. Vac. Sci. Technol. A* 39 (6) (2021) 060801, <http://dx.doi.org/10.1116/6.0001307>.
- [25] H. Mukaida, H. Okumura, J.H. Lee, H. Daimon, E. Sakuma, S. Misawa, K. Endo, S. Yoshida, Raman scattering of SiC: Estimation of the internal stress in 3C-SiC on Si, *J. Appl. Phys.* 62 (1987) <http://dx.doi.org/10.1063/1.339191>.
- [26] C. Kranert, C. Sturm, R. Schmidt-Grund, M. Grundmann, Raman tensor elements of β -Ga₂O₃, *Sci. Rep.* 6 (2016) <http://dx.doi.org/10.1038/srep35964>.
- [27] B.M. Janzen, P. Mazzolini, R. Gillen, A. Falkenstein, M. Martin, H. Tornatzky, J. Maultzsch, O. Bierwagen, M.R. Wagner, Isotopic study of Raman active phonon modes in β -Ga₂O₃, *J. Mater. Chem. C* 9 (2021) <http://dx.doi.org/10.1039/d0tc04101g>.
- [28] H.L. Huang, J.M. Johnson, C. Chae, A. Senckowski, M.H. Wong, J. Hwang, Atomic scale mechanism of β to γ phase transformation in gallium oxide, *Appl. Phys. Lett.* 122 (2023) <http://dx.doi.org/10.1063/5.0156009>.
- [29] M. Sarwar, R. Ratajczak, C. Mieszczynski, A. Wierzbicka, S. Gieraltowska, R. Heller, S. Eisenwinder, W. Wozniak, E. Guzewicz, Defect accumulation in β -Ga₂O₃ implanted with Yb, *Acta Mater.* 268 (2024) <http://dx.doi.org/10.1016/j.actamat.2024.119760>.
- [30] H. Li, S.H. Yuan, T.M. Huang, H.J. Chen, F.H. Lu, S. Zhang, D.S. Wu, Impact of thermal-induced sapphire substrate erosion on material and photodetector characteristics of sputtered Ga₂O₃ films, *J. Alloys Compd.* 823 (2020) <http://dx.doi.org/10.1016/j.jallcom.2020.153755>.
- [31] C.H. Liao, K.H. Li, C.G. Torres-Castanedo, G. Zhang, X. Li, Wide range tunable bandgap and composition β -phase (AlGa)₂O₃ thin film by thermal annealing, *Appl. Phys. Lett.* 118 (2021) <http://dx.doi.org/10.1063/5.0027067>.
- [32] D. Parker, E.A. Sutura, I. Kuprov, N.F. Chilton, How the ligand field in lanthanide coordination complexes determines magnetic susceptibility anisotropy, paramagnetic NMR shift, and relaxation behavior, *Acc. Chem. Res.* 53 (2020) <http://dx.doi.org/10.1021/acs.accounts.0c00275>.
- [33] K. Lee, M.S. Ameen, L.M. Rubin, D.D. Roh, R. Hong, R.N. Reece, D. Yoon, Damage control of ion implantation for advanced doping process by using in-situ temperature control, *Mater. Sci. Semicond. Process.* 117 (2020) <http://dx.doi.org/10.1016/j.mssp.2020.105164>.
- [34] C. Borschel, M.E. Messing, M.T. Borgström, W. Paschoal, J. Wallentin, S. Kumar, K. Mergenthaler, K. Deppert, C.M. Canali, H. Pettersson, L. Samuelson, C. Ronning, A new route toward semiconductor nanospintronics: Highly Mn-doped GaAs nanowires realized by ion-implantation under dynamic annealing conditions, *Nano Lett.* 11 (2011) <http://dx.doi.org/10.1021/nl2021653>.
- [35] X. Tang, Q. Han, X. Zhao, H. Song, K. Ren, T. Liu, Method for estimating the Stark splitting of rare-earth ions from the measured cross-section spectra, *Appl. Opt.* 57 (2018) <http://dx.doi.org/10.1364/ao.57.008573>.